Article

Operando identification of the oxide path mechanism with different dual-active sites for acidic water oxidation

Qianqian Ji[1,2,8], Bing Tang[3,8], Xilin Zhang[4,8], Chao Wang [3], Hao Tan [3], Jie Zhao[2], Ruiqi Liu[3], Mei Sun[5], Hengjie Liu [3], Chang Jiang[6], Jianrong Zeng[7], Xingke Cai [2] ✉ & Wensheng Yan [3] ✉

The microscopic reaction pathway plays a crucial role in determining the electrochemical performance. However, artificially manipulating the reaction pathway still faces considerable challenges. In this study, we focus on the classical acidic water oxidation based on RuO_2 catalysts, which currently face the issues of low activity and poor stability. As a proof-of-concept, we propose a strategy to create local structural symmetry but oxidation-state asymmetric $Mn^{4-\delta}$-O-$Ru^{4+\delta}$ active sites by introducing Mn atoms into RuO_2 host, thereby switching the reaction pathway from traditional adsorbate evolution mechanism to oxide path mechanism. Through advanced *operando* synchrotron spectroscopies and density functional theory calculations, we demonstrate the synergistic effect of dual-active metal sites in asymmetric $Mn^{4-\delta}$-O-$Ru^{4+\delta}$ microstructure in optimizing the adsorption energy and rate-determining step barrier via an oxide path mechanism. This study highlights the importance of engineering reaction pathways and provides an alternative strategy for promoting acidic water oxidation.

Hydrogen is a clean energy carrier with a high gravimetric energy density. Utilizing the electricity generated via renewable resources, such as wind and solar energy, for converting and storing hydrogen energy is an effective approach to address the fossil fuel crisis[1–3]. Currently, proton exchange membrane water electrolysis (PEMWE) technology is widely acknowledged as a promising and sustainable route for green hydrogen fuel production owing to its numerous merits, including high purity, high current density, low ohm resistance and perfect compatibility with renewable energy[4,5]. However, the anodic oxygen evolution reaction (OER) is a challenge to PEMWE, due to its intrinsic sluggishness in the four-electron transfer process[6]. Thus, developing efficient OER electrocatalysts is crucial for improving

the efficiency of PEMWE devices and further advancing their adoption and applicability.

Over the past decades, Ru-based electrocatalysts have demonstrated tremendous potential toward OER in acidic environments owing to the presence of Ru sites with diverse coordination environment on their surfaces, which remarkably influence the adsorption/desorption energy of the intermediates[7,8]. Further, the intrinsic activity of Ru sites in commercial RuO_2 requires an overpotential of approximately 330 mV to achieve 10 mA cm^{-2} current density in acidic environments. However, it suffers from severe dissolution and corrosion during OER in acidic media. Therefore, achieving simultaneous enhancement of the activity and stability of

[1]College of Civil and Transportation Engineering, Shenzhen University, Shenzhen, China. [2]Institute for Advanced Study (IAS), Shenzhen University, Shenzhen, China. [3]National Synchrotron Radiation Laboratory, University of Science and Technology of China, Hefei, China. [4]School of Physics, Henan Key Laboratory of Advanced Semiconductor & Functional Device Integration, Henan Normal University, Xinxiang, China. [5]Hefei National Research Center for Physical Sciences at the Microscale, University of Science and Technology of China, Hefei, China. [6]College of Energy, Xiamen University, Xiamen, China. [7]Shanghai Synchrotron Radiation Facility, Shanghai Advanced Research Institute, Chinese Academy of Sciences, Shanghai, China. [8]These authors contributed equally: Qianqian Ji, Bing Tang, Xilin Zhang. ✉e-mail: cai.xingke@szu.edu.cn; ywsh2000@ustc.edu.cn

Ru-based electrocatalysts for their applicability in PEMWE is an arduous task[9,10].

There are two primary OER mechanisms in acidic solutions[11]. The first one is the traditional adsorbate evolution mechanism (AEM). AEM exhibits an inherent linear relationship between the adsorption energy and the adsorption of *OH and *OOH active intermediates species, revealing a minimum theoretical overpotential of approximately 0.37 V, thereby constraining the advancement of efficient electrocatalysts[12–14]. Additionally, the oxidation of Ru metal atoms to high-valence soluble $RuO_2(OH)_2$ or RuO_4 species under strong acidic and oxidizing environment is detrimental to their long-time stability[15–18]. The second mechanism is the kinetically favorable lattice oxygen mechanism (LOM). This mechanism avoids the generation of *OOH intermediates, but it uses lattice oxygen to release oxygen products and forms lattice oxygen vacancies, which disrupt the thermally stable crystal structure[19,20]. Based on the reaction process analysis, the theoretical limitations of AEM and structurally unstable LOM result in inferior activity and stability, thereby restricting the practical application of Ru-based electrocatalyst in acidic media.

Recently, oxide path mechanism (OPM) has been discovered for OER that enables the direct coupling of adsorbed oxygen species (*O-O*) to release O_2, which effectively overcomes the scaling relationship limitation and maintains a complete thermally stable structure (Fig. 1)[21,22]. Previous reports claimed that the OPM in acidic is based only on the as-formed intermediates *O-O* and the theoretical simulation of the dual-active sites[22–24]. However, the exact underlying structural character of OPM, exhibiting good activity and stability, is still not entirely understood[25]. Uncovering the exact structural character of OPM and elucidating the exact function of each atom in the microstructure is highly desirable for artificially designing high-performance OPM catalysts in acidic solutions.

In this work, we partially substitute the Ru atoms in RuO_2 host with Mn atoms at the optimal composition to form a unique $Mn^{4-\delta}$-O-$Ru^{4+\delta}$ microstructure over the $Mn_{0.2}RuO_2$. We observe a strong signal assigned to *O-O* species, a typical intermediate for OPM on $Mn_{0.2}RuO_2$ during the OER in an acidic electrolyte using *operando* synchrotron radiation Fourier transform infrared spectroscopy (SR-FTIR). In contrast, the *OOH intermediate, a typical intermediate for AEM, is observed on RuO_2 with a Ru-O-Ru active center. The *operando* differential electrochemical mass spectrometry (DEMS) reveals the OER pathway switches after incorporating Mn atoms. Furthermore, we determine both Mn and Ru as dual-active centers for the OPM pathway by *operando* X-ray absorption fine spectroscopy (XAFS) and differential delta-XAFS (ΔXAFS) spectra analysis. Density functional theory (DFT) calculations reveal that the presence of Mn atoms in the $Mn_{0.2}RuO_2$ induce a charge redistribution in the $Mn^{4-\delta}$-O-$Ru^{4+\delta}$ microstructure, which facilitates the *OH adsorption and the charge transfer in $Mn_{0.2}RuO_2$. This results in a lower energy barrier for the direct connecting between two O* on the neighboring Mn/Ru sites, favoring the formation of a bridge *O-O* intermediate on the Mn-O-Ru microstructure, rather than absorbing one *OH into the neighboring *O to form a *OOH intermediate. This study provides a clear understanding of the OPM pathway based on the microstructural and electronic structure changes in the material, thus giving additional insights into the manual design of OPM catalysts from a structure viewpoint.

Results

Structural characterization to identify the $Mn^{4-\delta}$-O-$Ru^{4+\delta}$ pair

The $Mn_{0.2}RuO_2$ electrocatalyst was prepared by incorporating Mn atoms into the RuO_2 host via a hydrothermal reaction and subsequent annealing process (Fig. 2a and Supplementary Fig. 1). The bulk crystal structure and morphology of the obtained $Mn_{0.2}RuO_2$ were characterized using X-ray diffraction (XRD), scanning electron microscopy (SEM), and transmission electron microscopy (TEM). The XRD pattern of Mn-doped RuO_2 exhibits characteristic diffraction peaks identical to those of rutile p-RuO_2 (PDF#40-1290), indicating the absence of manganese oxide impurities and confirming the formation of a Mn-doped RuO_2 octahedral rutile phase (Fig. 2b). SEM images in Fig. 2c and Supplementary Fig. 2 reveal an array of nanorods for $Mn_{0.2}RuO_2$. The TEM image displays the uniformity of the $Mn_{0.2}RuO_2$ nanorods with a length of approximately 55 nm (Supplementary Fig. 2). The energy dispersive spectroscopy (EDS) elemental mapping images display an even distribution of Mn, Ru, and O elements in $Mn_{0.2}RuO_2$. From the EDS line-scanning and EDS spectra, the Mn/Ru atom ratio within the nanorods can be calculated to be approximately 1:4.6, which is close to our input ratio 1:5 (Fig. 2e and Supplementary Fig. 3). The inductively coupled plasma-mass spectrometry (ICP-MS) measurement further confirm the atom ratio of Mn: Ru is around 1:5 (Supplementary Table 1).

High-resolution TEM (HRTEM) image exhibits a lattice pattern corresponding to the (110) plane of $Mn_{0.2}RuO_2$ (Supplementary Fig. 4). In comparison with p-RuO_2, the introduction of Mn atom does not change the morphology of the nanorods in $Mn_{0.2}RuO_2$
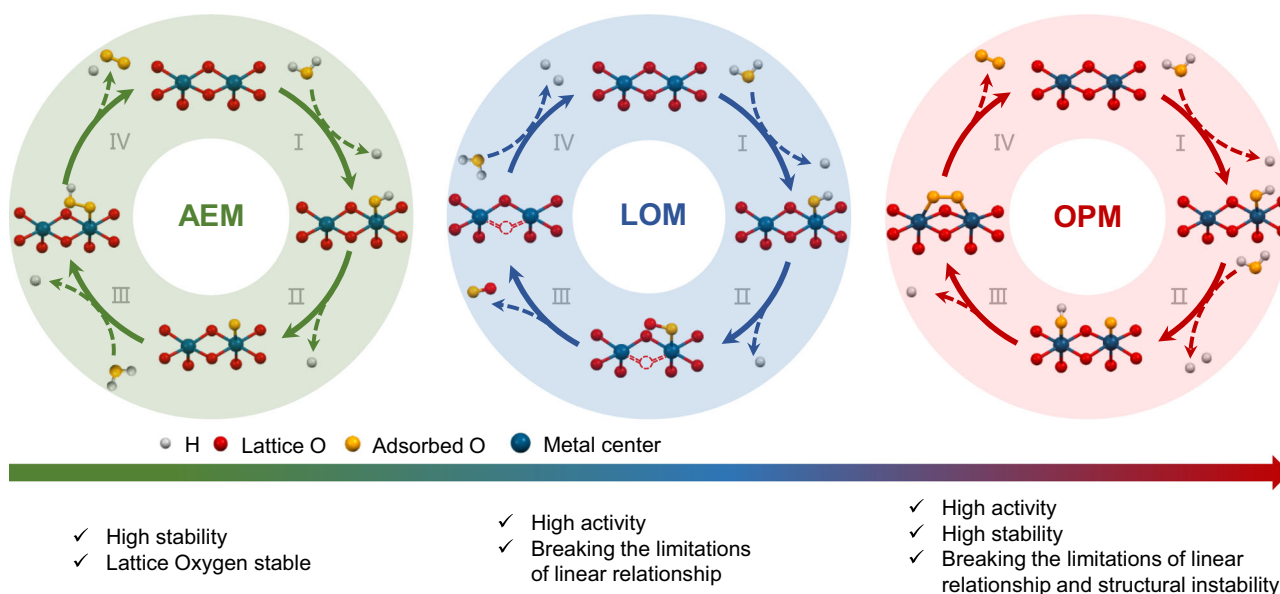

Fig. 1 | A survey of the catalytic reaction pathway and its charactersitics of RuO_2, including AEM, LOM and OPM.
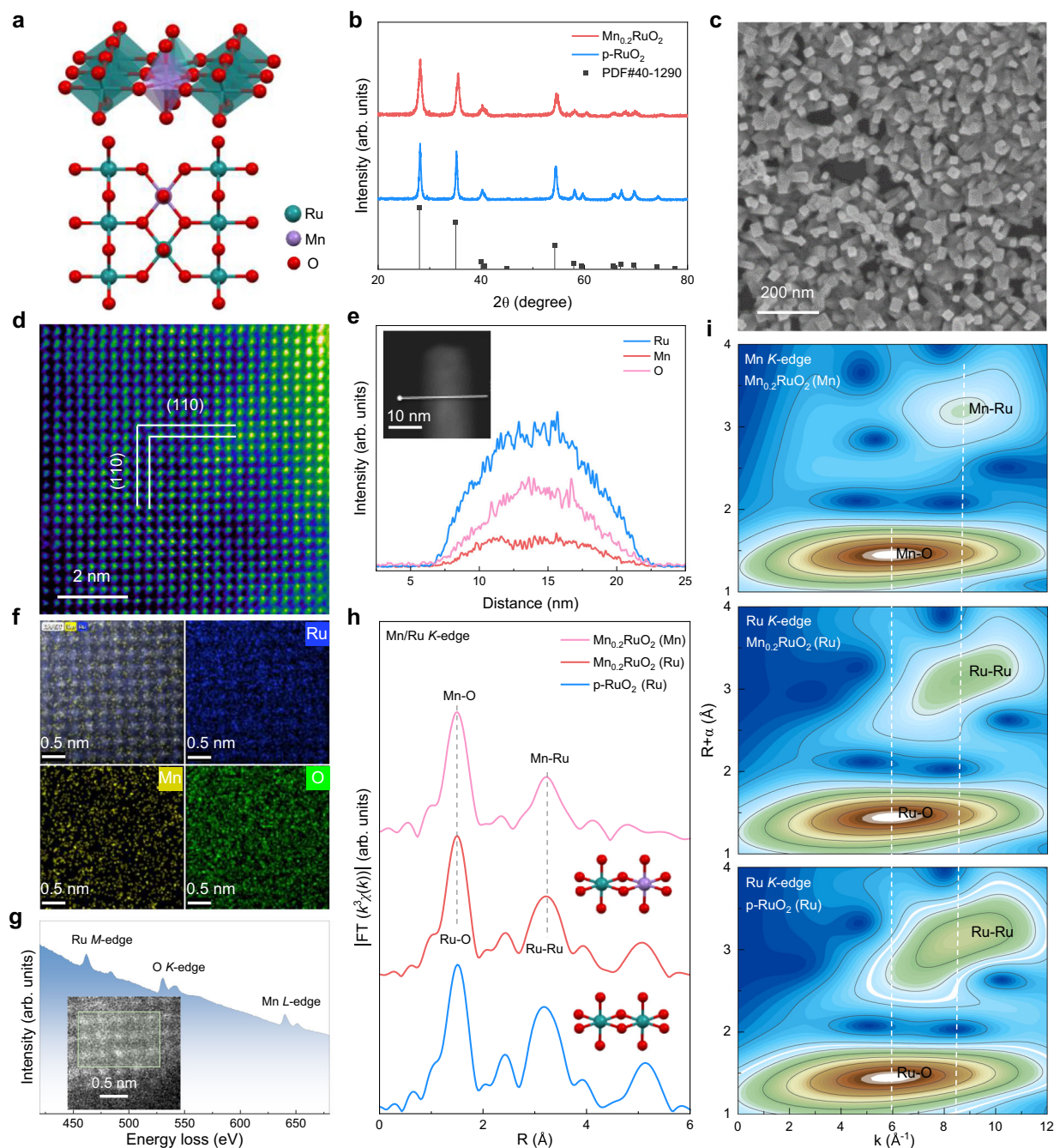
H   Lattice O   Adsorbed O   Metal center

✓ High stability
✓ Lattice Oxygen stable

✓ High activity
✓ Breaking the limitations of linear relationship

✓ High activity
✓ High stability
✓ Breaking the limitations of linear relationship and structural instability

Fig. 2 | Fine-structure characterization of Mn$_{0.2}$RuO$_2$. a Schematic diagram of the structure for Mn$_{0.2}$RuO$_2$. **b** The XRD patterns of Mn$_{0.2}$RuO$_2$ and p-RuO$_2$. **c** SEM image of Mn$_{0.2}$RuO$_2$. **d** Atomic-scale HAADF-STEM image of Mn$_{0.2}$RuO$_2$. **e** EDX linear-scanning elemental distribution of Mn, Ru and O for the Mn$_{0.2}$RuO$_2$. Inset: line-scanning TEM image. **f** Atomic-scale HAADF-STEM image and the corresponding EDS elemental mapping images for Mn$_{0.2}$RuO$_2$. **g** EELS spectra of Ru *M*-edge, O *K*-edge, and Mn *L*-edge for Mn$_{0.2}$RuO$_2$. Inset: HADDF-STEM image. **h** FT k^3-weighted Mn and Ru *K*-edge EXAFS spectra. **i** WT analysis of EXAFS spectra for Mn$_{0.2}$RuO$_2$ and p-RuO$_2$.

(Supplementary Figs. 5–6). Atomic level resolved high-angle dark-field imaging-scanning transmission electron microscopy (HAADF-STEM) and micro-structure sensitive extended XAFS (EXAFS) were performed to identify the local environment of Mn atoms within the RuO$_2$ lattice. The HAADF-STEM images show a regular arrangement of metal atoms (Mn/Ru) and no crystal lattice of individual manganese oxides in Mn$_{0.2}$RuO$_2$ (Fig. 2d and Supplementary Fig. 7). The lattice fringes could be attributed to the (110) plane of the octahedral structure, indicating that Mn atoms are successfully substituted into the RuO$_2$ crystal lattice[26]. Additionally, three random regions EDS elemental mapping images confirm the atomic-scale uniform

distribution of Mn and Ru atoms (Fig. 2f and Supplementary Fig. 8). Electron energy-loss spectroscopy (EELS) in the selected area clearly exhibits Ru *M*-edge, O *K*-edge and Mn *L*-edge spectra, suggesting that Mn atoms are located at the original Ru positions (Fig. 2g).

Subsequently, we conducted a detailed analysis of the Fourier transform (FT) curves of the Mn and Ru *K*-edge EXAFS $k^3\chi(k)$ functions for Mn$_{0.2}$RuO$_2$. The Mn *K*-edge FT-EXAFS spectra of standard MnO, Mn$_2$O$_3$, MnO$_2$ and Mn$_{0.2}$RuO$_2$, as well as the Ru *K*-edge FT-EXAFS spectra of p-RuO$_2$ and Mn$_{0.2}$RuO$_2$ are given in Fig. 2h and Supplementary Fig. 9. The FT-EXAFS curves of the Mn *K*-edge EXAFS spectra for Mn$_{0.2}$RuO$_2$ show intense peaks located at approximately 1.5 and
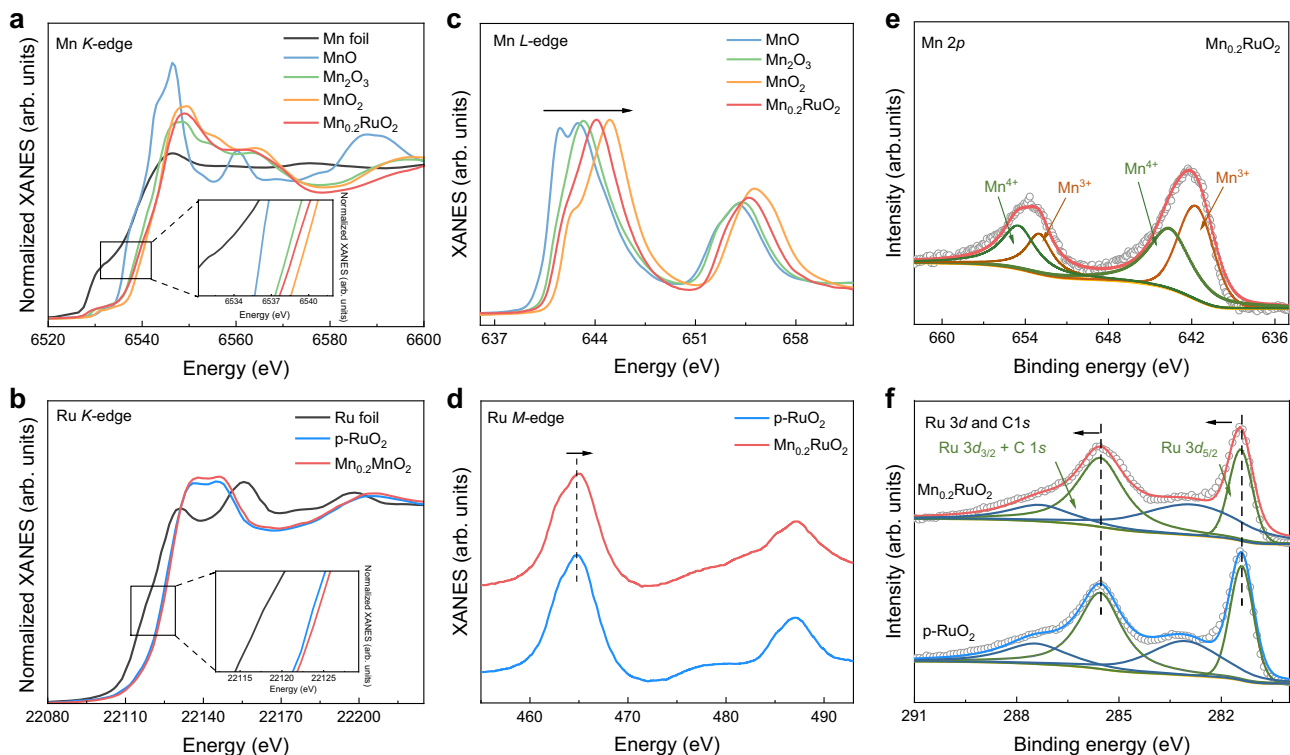
Fig. 3 | Electronic structure characterization of Mn$_{0.2}$RuO$_2$. a Mn K-edge XANES spectra of Mn foil, MnO, Mn$_2$O$_3$, MnO$_2$ and Mn$_{0.2}$RuO$_2$. Inset: magnified XANES spectra. **b** Ru K-edge XANES spectra of Ru foil, p-RuO$_2$ and Mn$_{0.2}$RuO$_2$. Inset: magnified XANES spectra. **c** Mn L-edge XANES spectra of MnO, Mn$_2$O$_3$, MnO$_2$ and Mn$_{0.2}$RuO$_2$. The arrow points to the high energy direction. **d** Ru M-edge XANES spectra of p-RuO$_2$ and Mn$_{0.2}$RuO$_2$. The arrow points to the high energy direction. **e** Mn $2p$ XPS spectra of Mn$_{0.2}$RuO$_2$. **f** Ru $3d$ and C $1s$ XPS spectra of p-RuO$_2$ and Mn$_{0.2}$RuO$_2$. The arrow points to the high binding energy direction.

3.2 Å, corresponding to the Mn-O and Mn-Ru scattering, respectively. These observations closely resemble the features of Ru K-edge FT-EXAFS spectra in Mn$_{0.2}$RuO$_2$ and p-RuO$_2$; however, they differ from the characteristics of standard manganese oxide, indicating that the introduced Mn atoms occupy the same crystal lattice environment as that of the Ru atoms, thereby preserving the symmetric arrangement of the RuO$_2$ octahedral structure. To determine the specific coordination numbers of various paths, the FT-EXAFS spectra were reasonably fitted (Supplementary Fig. 10 and Supplementary Table 2). The best-fitting results illustrate the similar local environment of Mn and Ru atoms in Mn$_{0.2}$RuO$_2$. Furthermore, the wavelet transform (WT) EXAFS analysis provided additional insights into the local bonding environment. The Mn K-edge WT plots of Mn$_{0.2}$RuO$_2$ reveal the maximum WT value at approximately 6.0 Å^{-1} ascribed to the bonding between Mn and light O atoms in first shell, and the maximum WT value at approximately 8.5 Å^{-1} associated with the scattering between Mn and heavy Ru atoms in high shell (Fig. 2i). Consequently, combining the Mn and Ru K-edge WT plots of Mn$_{0.2}$RuO$_2$ and p-RuO$_2$ demonstrates that the Mn atoms precisely replace the lattice positions of the Ru atoms and the local coordinate environments of Mn-O-Ru and Ru-O-Ru are nearly identical.

To determine the oxidation states of Mn and Ru atoms in the presence of Mn atoms in Mn$_{0.2}$RuO$_2$, X-ray absorption near-edge structure (XANES) and X-ray photoelectron spectra (XPS) analyzes were carried out. In the Mn K-edge XANES spectra, the absorption edge of Mn$_{0.2}$RuO$_2$ shifts marginally towards a higher photon energy compared to those of MnO and Mn$_2$O$_3$; however, it is lower than that of MnO$_2$, demonstrating that the oxidation state of Mn ranges between +3 and +4 (Fig. 3a). Furthermore, The Mn K-edge XANES spectra of Mn$_{0.2}$RuO$_2$ exhibit a shape that is markedly different from the reference samples. Meanwhile, Mn$_{0.2}$RuO$_2$ displays a similar geometry structure but optimized electron structure relative to that of p-RuO$_2$ in

the O K-edge spectra, consistent with the Ru K-edge EXAFS results (Supplementary Fig. 11). Figure 3b shows a shift in the absorption edge of Ru K-edge for Mn$_{0.2}$RuO$_2$ to a higher energy position compared to that of p-RuO$_2$, suggesting that the introduction of Mn atoms leads to an electron redistribution around Ru. This leads to the oxidation state of Ru in Mn$_{0.2}$RuO$_2$ exceeds +4. Moreover, the O $1s$ XPS spectra also confirm that the oxidation state of Ru is higher in Mn$_{0.2}$RuO$_2$ than in p-RuO$_2$ (Supplementary Fig. 12). The Mn L-edge XANES spectra of Mn$_{0.2}$RuO$_2$ reveals that the absorption peak of Mn$_{0.2}$RuO$_2$ lies between those of Mn$_2$O$_3$ and MnO$_2$, indicating that the oxidation state of Mn in Mn$_{0.2}$RuO$_2$ is below +4 (Fig. 3c). Similarly, the Ru M-edge spectra display a blue shift in accordance with the results of the Ru K-edge XANES analyzes (Fig. 3d). The XPS spectra of Mn $2p$ in Mn$_{0.2}$RuO$_2$ further indicates that the oxidation state is below +4, denoted as Mn$^{4+\delta}$ (Fig. 3e). In the Ru $3d$ and C1s XPS spectra of RuO$_2$ and Mn$_{0.2}$RuO$_2$, two sets of doublet peaks are observed between 280 and 290 eV, corresponding to the peaks of Ru^{4+} $3d_{5/2}$ and $3d_{3/2}$ + C 1s, respectively. The Ru $3d$ and C 1s XPS peak of Mn$_{0.2}$RuO$_2$ is slightly shifted to a higher binding energy compared to that of p-RuO$_2$, further confirming the presence of higher valence Ru species in Mn$_{0.2}$RuO$_2$, denoted as Ru$^{4+\delta}$ (Fig. 3f). Specifically, through linear fitting of Mn and Ru K-edge XANES spectra for Mn$_{0.2}$RuO$_2$ and the reference samples, the oxidation states of Mn and Ru is estimated to be +3.55 and +4.46, respectively, in Mn$_{0.2}$RuO$_2$ (Supplementary Fig. 13). These findings provide detailed evidence that electrons are transferred from Ru atoms to neighboring Mn atoms through bridging O atoms, forming unique localized Mn$^{4-\delta}$-O-Ru$^{4+\delta}$ pairs.

OER performance of Mn$_{0.2}$RuO$_2$ electrocatalyst

The OER measurements were used to characterize the Mn$_x$RuO$_2$ and p-RuO$_2$ to determine the effect of the Mn$^{4-\delta}$-O-Ru$^{4+\delta}$ microstructure on the electrocatalytic performance. We synthesized samples with
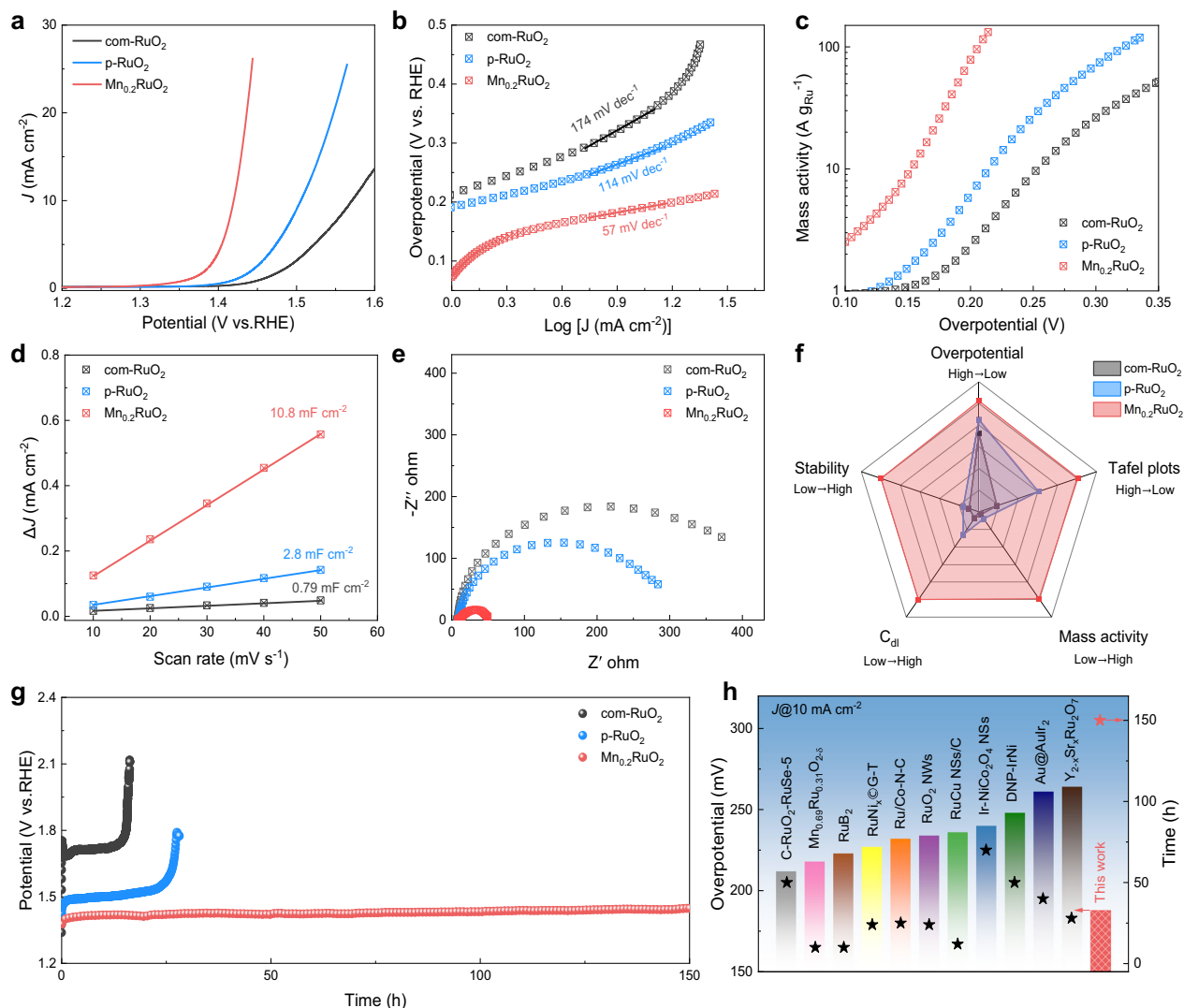
Fig. 4 | Activity and stability measurement. a The LSV curves of com-RuO_2, p-RuO_2, and $Mn_{0.2}RuO_2$ with 85% *iR* compensation in 0.5 M H_2SO_4 (pH = 0) with a scan rate of 10 mV s^{-1} at room temperature. **b** Tafel slopes and (**c**) mass activity of com-RuO_2, p-RuO_2 and $Mn_{0.2}RuO_2$. **d** C_{dl} plots derived from the fitting CV curves at difference scan rates. **e** EIS Nyquist plots of com-RuO_2, p-RuO_2 and $Mn_{0.2}RuO_2$ measured at the same potential. **f** Comprehensive comparison of the OER performance for $Mn_{0.2}RuO_2$ and our reference samples. **g** The constant current tests at 10 mA cm^{-2} for com-RuO_2, p-RuO_2 and $Mn_{0.2}RuO_2$. **h** Comparison of $Mn_{0.2}RuO_2$ with previously reported Ru/Ir-based electrocatalysts in terms of overpotential and stability at 10 mA cm^{-2} in 0.5 M H_2SO_4, at room temperature.

different Mn doping levels, namely, $Mn_{0.1}RuO_2$, $Mn_{0.2}RuO_2$, and $Mn_{0.3}RuO_2$, and filtered them using linear sweep voltammetry (LSV) curves with *iR*-corrected. Among them, $Mn_{0.2}RuO_2$ exhibits an overpotential of 188 mV at a current density of 10 mA cm^{-2}, outperforming $Mn_{0.1}RuO_2$, $Mn_{0.3}RuO_2$, p-RuO_2 and commercial RuO_2 (referred to as com-RuO_2) (Fig. 4a and Supplementary Figs. 14–15). The Tafel slope plots derived from LSV curves display that the Tafel slope of p-RuO_2 is 114 mV dec^{-1}, which is smaller than that of com-RuO_2, potentially attributed to differences in particle size. Among them, $Mn_{0.2}RuO_2$ shows the lowest Tafel slope, suggesting that the unique $Mn^{4-\delta}$-O-$Ru^{4+\delta}$ structure could improve the OER kinetics (Fig. 4b). Moreover, the mass activity of $Mn_{0.2}RuO_2$ is 47.7 A g^{-1}, which surpasses those of p-RuO_2 (4.2 A g^{-1}) and com-RuO_2 (1.7 A g^{-1}) at an overpotential of 188 mV, highlighting the optimal activity of $Mn_{0.2}RuO_2$ under acidic OER conditions (Fig. 4c).

Next, we performed cyclic voltammetry at different scan rates to obtain double-layer capacitance (C_{dl}) and evaluate the electrochemical active surface area (ECSA) for OER activity (Supplementary Fig. 16)[27]. The $Mn_{0.2}RuO_2$ and p-RuO_2 show a similar morphology, however, the C_{dl} value of $Mn_{0.2}RuO_2$ is nearly 4 times higher than that

of p-RuO_2 (Fig. 4d). To consider the intrinsic activity of each active site, we normalized the LSV curves using both the ECSA and metal mass activity. Significantly, $Mn_{0.2}RuO_2$ still exhibits a lower overpotential than p-RuO_2, illustrating that doping Mn into the RuO_2 lattice is an effective approach to enhance the intrinsic activity of each metal site (Supplementary Fig. 17)[28]. The BET normalized TOF also support the higher intrinsic activity of $Mn_{0.2}RuO_2$ (Supplementary Figs. 18–19)[29]. Through online gas chromatography testing, it was demonstrated that $Mn_{0.2}RuO_2$ achieves a high OER Faradic efficiency exceeding 99% and 98% at current density of 10 mA cm^{-2} and 30 mA cm^{-2} for OER, respectively (Supplementary Fig. 20 and Supplementary Table 3). Additionally, electrochemical impedance spectroscopy (EIS) was performed on all samples at 1.45 V versus RHE, which reveals that the $Mn_{0.2}RuO_2$ displays the smallest charge transfer resistance (Fig. 4e)[30]. Moreover, the two-probe van der Pauw method was conducted at room temperature to analyze the conductivity capability of the electrocatalysts. The electronic conductivity of $Mn_{0.2}RuO_2$ is 3.3 S cm^{-1}, considerably superior to those of p-RuO_2 (1.98 S cm^{-1}) and com-RuO_2 (0.52 S cm^{-1}), inferring that an asymmetric $Mn^{4-\delta}$-O-$Ru^{4+\delta}$ structure facilitates the electron transfer in

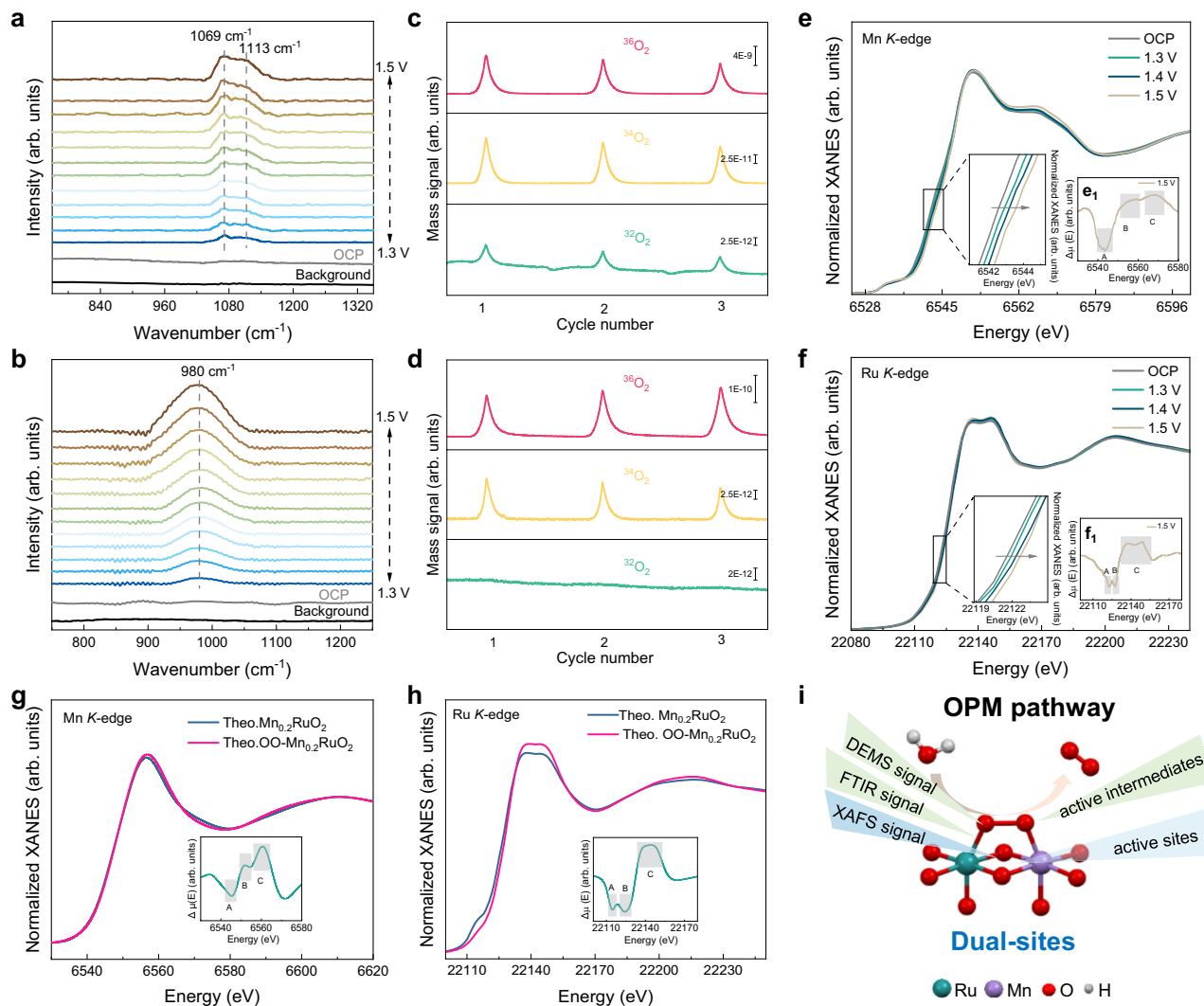**Fig. 5 | Operando SR-FTIR, DEMS, XAFS measurements. a, b** *Operando* SR-FTIR spectra for $Mn_{0.2}RuO_2$ (**a**) and p-RuO_2 (**b**). **c, d** *Operando* DEMS signals of $^{32}O_2$, $^{34}O_2$ and $^{36}O_2$ for (**c**) $Mn_{0.2}RuO_2$ and (**d**) p-RuO_2. **e, f** *Operando* Mn (**e**) and Ru (**f**) *K*-edge XANES spectra. Inset: magnified XANES spectra, and experimental Mn (**e$_1$**) and Ru *K*- edge (**f$_1$**) ΔXANES spectra. **g, h** Theoretical Mn (**g**) and Ru (**h**) *K*-edge spectra of $Mn_{0.2}RuO_2$ and OO-$Mn_{0.2}RuO_2$ (a model of *O-O* key intermediate absorption on the $Mn_{0.2}RuO_2$ surface) Inset: theoretical Mn and Ru *K*-edge ΔXANES spectra. **i** Schematic of the OPM pathway for $Mn_{0.2}RuO_2$.

the sample (Supplementary Fig. 21). Therefore, a comprehensive analysis suggests that $Mn_{0.2}RuO_2$ demonstrates excellent OER activity, attributed to its outstanding reaction kinetics, mass activity, charge transfer, and electrical conductivity.

The durability of the electrocatalysts in acid is another crucial performance parameter for OER, which has been evaluated using chronopotentiometry stability test. Compared to the fast potential enhancement for p-RuO_2 and com-RuO_2, $Mn_{0.2}RuO_2$ manifests almost no obvious decays over 150 h operation at 10 mA cm^{-2} (Fig. 4g). Furthermore, $Mn_{0.2}RuO_2$ exhibits only a slight increase of 50 mV in potential over a duration of 95 h at 50 mA cm^{-2}, demonstrating significantly improved acidic stability (Supplementary Fig. 22). ICP-MS was used to obtain quantitative information on Ru and Mn dissolution during the OER process (Supplementary Table 4). Notably, introducing Mn atoms into RuO_2 lattice reduces the dissolution of Ru atoms to 1.3% after a 20 h durability test, which is significantly lower than previously reported Ru-based oxides (Supplementary Fig. 23)[9]. The stability number (S-number) of $Mn_{0.2}RuO_2$ represents improvement by an order of magnitude compared to p-RuO_2[31,32], and $Mn_{0.2}RuO_2$ exhibits higher S-number than other Ru/ Ir-based electrocatalysts previously reported (Supplementary Fig. 24

and Supplementary Tables 5-6). These results reveal that $Mn_{0.2}RuO_2$ exhibits outstanding resistance to corrosion and dissolution under acidic condition, which can be attributed to the unique electron structure of the $Mn^{4+\delta}$-O-$Ru^{4+\delta}$ pairs.

The structural integrity of the $Mn_{0.2}RuO_2$ after OER was further examined. The morphological structure of $Mn_{0.2}RuO_2$ maintains its initial state, while metal vacancies were observed up to three atomic layers on the surface, as shown in Supplementary Figs. 25–27. To clarify the electronic structure of $Mn_{0.2}RuO_2$ after OER, XPS fitted areas were employed. The calculation results reveal that the local Mn^{4+} domains were formed after the OER testing (Supplementary Fig. 28 and Supplementary Table 7). Analyzes of the XPS and XANES spectra reveal that the increase of oxidation states for both Mn and Ru due to these as formed metal vacancies on the surface, whereas the octahedral structure remains stable. Meanwhile, no oxygen vacancies generated after the OER process (Supplementary Figs. 28-29). Additionally, we compared the overpotential at 10 mA cm^{-2} and long-time stability of $Mn_{0.2}RuO_2$ with recently reported Ru/Ir-based oxide OER catalysts in acidic media to evaluate their performance relative to those of state-of-art OER catalysts (Fig. 4h)[19,33–42]. Meanwhile, we also compared the recorded overpotentials to reach a
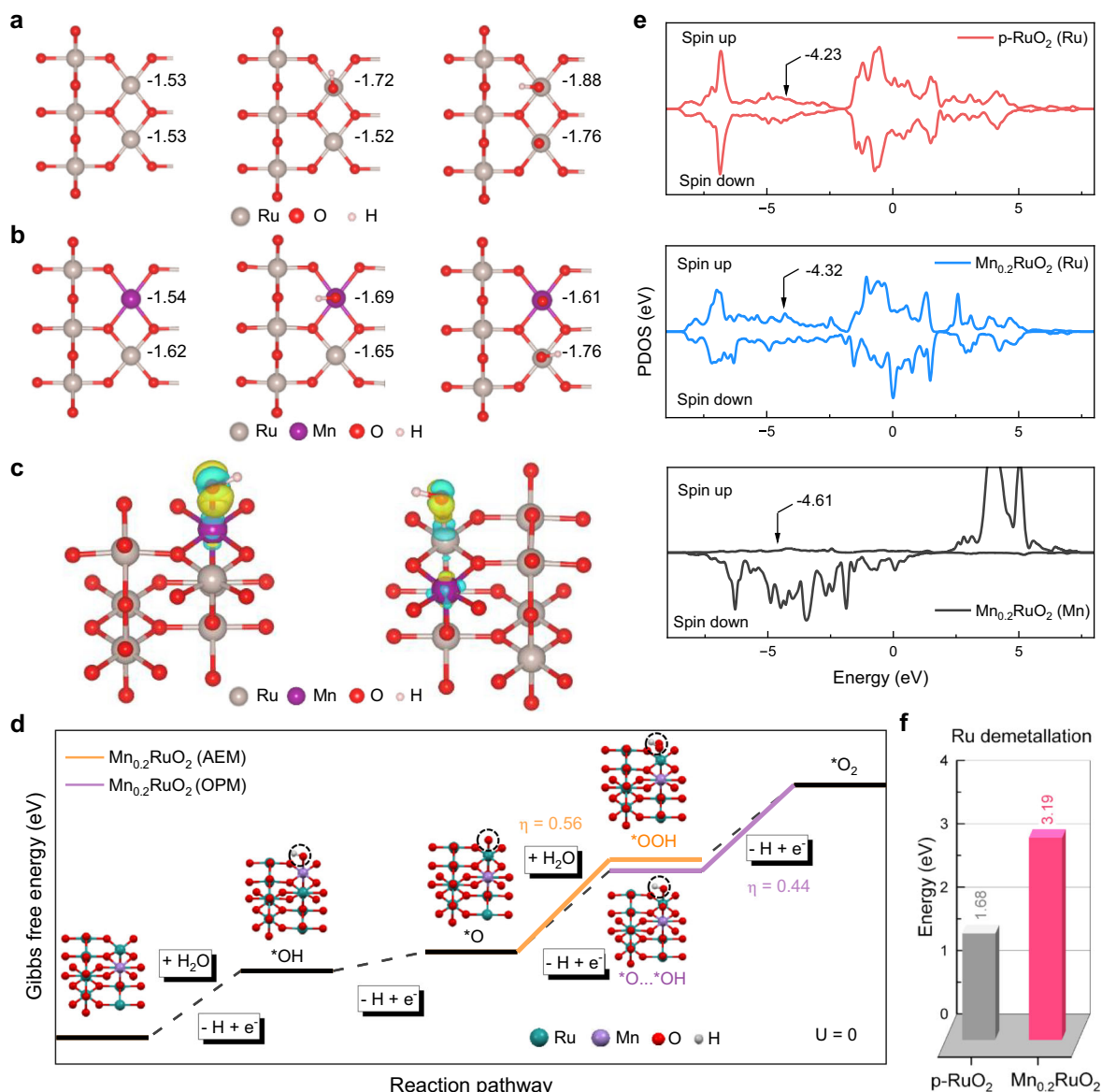
Fig. 6 | OER mechanism analysis. a, b Bader charge analysis for p-RuO$_2$ (**a**) and Mn$_{0.2}$RuO$_2$ (**b**). **c** Differential charge density analysis of adsorption *OH on Ru atom (left) and Mn (right) atom for Mn$_{0.2}$RuO$_2$. **d** Gibbs free energy diagram for AEM path and OPM path on the surface of Mn$_{0.2}$RuO$_2$. **e** PDOS and *d*-band center of Ru 4*d* (−4.23) for p-RuO$_2$, Ru 4*d* (−4.32) and Mn 3*d* (−4.61) for Mn$_{0.2}$RuO$_2$. Corresponding *d*-band centers are denoted by arrows. **f** Calculated energy for Ru demetallation of p-RuO$_2$ and Mn$_{0.2}$RuO$_2$.

specific mass-normalized current density for the catalysts (Supplementary Fig. 30 and Supplementary Table 8). The above results demonstrate that the Mn$_{0.2}$RuO$_2$ electrocatalyst with Mn$^{4+\delta}$-O-Ru$^{4+\delta}$ structure shows better activity and higher stability than that of the RuO$_2$ with the Ru-O-Ru structure.

In addition, we also assembled a PEM electrolyzer utilizing a Nafion 115 proton exchange membrane, with p-RuO$_2$/Mn$_{0.2}$RuO$_2$ as the anode electrocatalysts and commercial Pt/C as the cathode electrocatalysts. The current-voltage (I-V) characteristic polarization curves show that the Mn$_{0.2}$RuO$_2$ based PEM electrolyzer achieves a high current density of 1 A cm^{-2} at a cell voltage of 1.69 V, outperforming p-RuO$_2$ based one, which requires a 1.90 V cell voltage to reach 1 A cm^{-2}. Meanwhile, p-RuO$_2$ based PEM electrolyzer lost activity within 40 h at a current of 200 mA cm^{-2}, while the Mn$_{0.2}$RuO$_2$ based PEM electrolyzer can be maintained for 180 h, indicating the potential for practical application of the Mn$_{0.2}$RuO$_2$ electrocatalyst (Supplementary Fig. 31 and Supplementary Table 9).

Elucidating the OER mechanism for the Mn$^{4+\delta}$-O-Ru$^{4+\delta}$ microstructure sample using *operando* characterizations

To understand the dynamic structural evolution and reaction pathway on the Mn$^{4+\delta}$-O-Ru$^{4+\delta}$ microstructure, *operando* characterizations, including *operando* SR-FTIR, *operando* DEMS, and *operando* XAFS, were used to identify the key intermediates on the Mn$^{4+\delta}$-O-Ru$^{4+\delta}$ microstructure and the reaction active sites during actual OER working conditions.

Operando SR-FTIR is highly sensitive to the vibrations of key reactive intermediates, providing nearly real-time visualization of the structural evolution under working potentials. Figure 5a shows the emergence of distinctive vibration frequencies at 1069 cm^{-1} and 1113 cm^{-1} with the applied potential gradually increases from 1.3–1.5 V in Mn$_{0.2}$RuO$_2$. Based on previous reports, the emergence of vibration bands approximately 1100 cm^{-1} can be assigned to the bridging oxygen configuration at the dual active site[22,25,43–47]. This potential-dependent SR-FTIR absorption band indicates that the key *O-O* intermediate emerges at the dual-metal active sites simultaneously, forming a

characteristic M-*O-O*-M configuration, suggesting that $Mn_{0.2}RuO_2$ follows an OPM pathway. For comparison, *operando* SR-FTIR measurements were also performed on p-RuO_2. Apparently, a single broad infrared vibration band at 980 cm^{-1} emerges with increasing applied potentials from 1.3-1.5 V. This vibration band could be attributed to the typical Ru-*OOH intermediate, illustrating that p-RuO_2 tends to follow a traditional AEM pathway (Fig. 5b)[47]. Additionally, *operando* DEMS with isotope labeling was carried out to validate the oxygen evolution mechanism, utilizing 0.5 M H_2SO_4 $H_2^{18}O$ as the electrolyte. The primary mass signals for p-RuO_2 are $^{34}O_2$ ($^{16}O^{18}O$) and $^{36}O_2$ ($^{18}O^{18}O$) products, while for $Mn_{0.2}RuO_2$ $^{32}O_2$ ($^{16}O^{16}O$), $^{34}O_2$ ($^{16}O^{18}O$) and $^{36}O_2$ ($^{18}O^{18}O$) were detected (Figs. 5c, d). It is worth noting that the presence of $^{32}O_2$ originates from surface oxygen adsorbates, and the direct coupling of two ^{16}O adsorbates results in the observation of $^{32}O_2$, a phenomenon exclusively observed in $Mn_{0.2}RuO_2$. The signal intensity of $^{36}O_2$ is two and three orders of magnitude higher than that for $^{32}O_2$ and $^{34}O_2$, respectively, indicating that the oxygen products primarily originate from two ^{18}O atoms in the isotope-labeled electrolyte. The Ru M-edge and Ru L_3-edge XANES spectra, which are sensitive to atomic structure, further exclude the possibility of a lattice oxygen mechanism pathway (Supplementary Fig. 32)[48]. These results also support the occurrence of dual-metal active sites via the OPM pathway in $Mn_{0.2}RuO_2$.

Operando XAFS technology was conducted to explore and gain active structure evolution information, due to its structure sensitivity. The Mn K-edge XANES spectra show a gradual positive shift in the absorption edge photon energy as the applied potential increases from OCP to 1.5 V, which indicates an increase in the Mn oxidation state, suggesting a partial electron transfer from Mn atoms to neighboring atoms or absorbed oxygen-containing species under potential-driven conditions (Fig. 5e). The Mn K-edge FT-EXAFS spectra shows that the main peak corresponds to first-shell of Mn-O coordination at approximately 1.5 Å. Interestingly, as the applied potential increases, the length of Mn-O bond remains nearly unchanged, indicating that lattice oxygen hardly participates in the OER process (Supplementary Figs. 33–34 and Supplementary Table 10)[4,49]. In the Ru K-edge XANES spectra, the adsorption edge position progressively increases as the applied potential is continuously raised in the oxidation reaction regions, resulting in higher oxidation states during the OER process (Fig. 5f). Analogously, the first-shell Ru-O bond remains at approximately 1.5 Å distance, and the change in potential does not affect the bond length between Ru and O atoms (Supplementary Figs. 33 and 35 and Supplementary Table 11). More importantly, to exclude the contribution of bulk materials and simultaneously amplify the signal response of the surface structural changes under operating conditions, delta-XAFS (ΔXAFS) spectra were introduced[50]. Based on the theory of multiple scattering, we simulated Mn and Ru K-edge XANES spectra based on the structure models of the initial and adsorbed key oxygen-containing (*O-O*) intermediates (Fig. 5g–h). The comparison between experimental and theoretical Mn K-edge ΔXANES spectra exhibits similar characteristic peaks, which are also observed in the Ru K-edge ΔXANES spectra. These results indicate that the subtle changes in the Mn and Ru K-edge XANES spectra under applied reaction potentials stem from the adsorption of oxygen-containing intermediates on Mn and Ru dual-metal active sites in $Mn_{0.2}RuO_2$. Moreover, we also simulated other non-bridging oxygen adsorption models, such as *OOH on the Ru atom and *O on the Mn atom. The theoretical ΔXANES spectra showed that this adsorption configuration do not match well with the experimental ΔXANES spectra, excluding other adsorbate configuration (Supplementary Fig. 36). Combined with *operando* SR-FTIR and *operando* DEMS results (Fig. 5i), it is evident the synergistic effect of both Mn and Ru atoms are involved the adsorption of oxygen-containing species and forming a characteristic Mn-*O-O*-Ru configuration of $Mn_{0.2}RuO_2$. This conclusion provides a deeper understanding on the catalytic mechanism transition from AEM to OPM.

DFT simulation to bridge the $Mn^{4+\delta}$-O-$Ru^{4+\delta}$ microstructure with the excellent OER performance via the OPM pathway

Density functional theory (DFT) calculations were performed to gain an insight into the origin of the OPM pathway and the excellent OER performance of $Mn^{4+\delta}$-O-$Ru^{4+\delta}$ microstructure in $Mn_{0.2}RuO_2$. The structural models of p-RuO_2 and $Mn_{0.2}RuO_2$ were constructed based on the HAADF-STEM and EXAFS results, where the exposed (110) surface forms the active crystal plane (Supplementary Figs. 37–38 and Supplementary Table 12). The atomic coordinates of the optimized computational models are provided in Supplementary Data 1. Bader charge analysis was utilized to explore the charge distribution on the p-RuO_2 and $Mn_{0.2}RuO_2$ surfaces. The substitution of Ru with Mn atoms in $Mn_{0.2}RuO_2$ leads to a remarkable alteration in the positive valence of the nearest neighboring Ru atoms (Figs. 6a, b and Supplementary Fig. 39), which strongly supports the Ru $3d$ XPS and Ru K-edge XANES results, and the Ru atom in the Mn-O-Ru microstructure of $Mn_{0.2}RuO_2$ shows an oxidation state > +4. In p-RuO_2 with Ru-O-Ru microstructure, when *OH was adsorbed on one Ru site, the other Ru atom exhibits a limited valence state change (Fig. 6a). However, in $Mn_{0.2}RuO_2$ with $Mn^{4+\delta}$-O-$Ru^{4+\delta}$ microstructure, when *OH is adsorbed on the Mn site, the electron donating ability of Ru atom changes remarkably, indicating a strong electron exchange capability between Mn and Ru atoms (Fig. 6b). After the adsorption of the *OH and *O species, the Ru atom of Ru-O-Ru microstructure in p-RuO_2 losses about 1.88 |e| to *OH, which reduces to 1.76 |e| in the $Mn^{4+\delta}$-O-$Ru^{4+\delta}$ microstructure in $Mn_{0.2}RuO_2$. As a result, the over-oxidation of active Ru atoms into soluble species could be depressed in $Mn_{0.2}RuO_2$ (Fig. 6a–b).

The differential charge density and adsorption energy of the *OH species on the Ru and Mn sites were compared, which indicates that Mn atoms serve as the initial reaction sites in $Mn_{0.2}RuO_2$ (Fig. 6c and Supplementary Fig. 40). Hence, the unique $Mn^{4+\delta}$-O-$Ru^{4+\delta}$ structure shows optimal adsorption towards *OH species than the Ru-O-Ru microstructure. As shown in Fig. 6d, both the traditional AEM and dual-sites OPM pathways were considered for $Mn_{0.2}RuO_2$. In the AEM pathway, the rate-limiting step is the formation of *OOH intermediate at a single metal site, which has a higher free energy change of 0.56 eV. In the OPM pathway, the rate-limiting step shifts to *O-O* coupling and O_2 releasing process, which occurs on dual-sites with lower free energy of 0.44 eV, thus effectively reducing the energy barrier of the rate-limiting step. These results are consistent with the findings of *operando* XANES and *operando* SR-FTIR experiments, confirming that the OER follows the OPM pathway on the $Mn^{4+\delta}$-O-$Ru^{4+\delta}$ in $Mn_{0.2}RuO_2$. The Gibbs free energy assessment for both AEM and OPM pathways was performed for p-RuO_2 (Supplementary Fig. 41). The AEM pathway exhibits a lower energy barrier on the p-RuO_2 surface with the Ru-O-Ru microstructure, which agrees with the results of *operando* SR-FTIR.

Additionally, the partial densities of states (PDOS) analysis reveals that introduced Mn atoms could shift the Fermi level upwards, leading to the electron transfer from Ru to the Mn atom in $Mn_{0.2}RuO_2$ increases the valence state and is in agreement with the XANES and XPS results (Fig. 6e). The PDOS near the Fermi level increases for $Mn_{0.2}RuO_2$, indicating a higher availability of electron states for electron transfer, resulting in improved electrical conductivity. Furthermore, the introduction of Mn optimizes the d-band center of Ru, which facilitates the desorption of intermediate species. Finally, the corrosion resistance of p-RuO_2 and $Mn_{0.2}RuO_2$ was evaluated. The energy cost of Ru demetallation significantly increases from 1.68 to 3.19 eV with the substitution of Mn atoms into RuO_2 lattice, demonstrating that Mn incorporation stabilizes the lattice structure (Fig. 6f). Considering the experimental dissolution of Ru, we further calculated the Gibbs free energy change of $Mn_{0.2}RuO_2$ during the OER process via both the AEM and OPM pathways in the presence of Ru vacancy. Although vacancies affect the adsorption step of reactants, it is worth noting that following the OPM pathway still exhibits a lower energy barrier for the formation of key intermediates (Supplementary Fig. 42).

These findings illustrate that the introduction of Mn atoms enables a switch in the reaction pathway even considering the dissolution of Ru atoms during the OER process.

Discussion

In this work, we used advanced *operando* characterization to elucidate the reaction pathway transition from AEM to OPM owing to microstructural changes induced by substituting Ru atoms with the Mn in octahedral rutile RuO_2. We observed a key intermediate, *O-O*, during the OER process in $Mn_{0.2}RuO_2$ with $Mn^{4-\delta}$-O-$Ru^{4+\delta}$ microstructure using *operando* SR-FTIR, which is direct evidence for the OPM pathway. In contrast, only *OOH, a key intermediate in the AEM pathway, was observed in the p-RuO_2 with Ru-O-Ru microstructure. *Operando* DEMS also supported the presence of dual-metal active sites in $Mn_{0.2}RuO_2$, while the single-metal active site in p-RuO_2 during the OER process. Moreover, we identified both the Mn and Ru atoms as active sites in the $Mn^{4-\delta}$-O-$Ru^{4+\delta}$ dual-site structure, and form a bridge *O-O* intermediate using *operando* XANFS and ΔXANES spectra. This change in the reaction pathway remarkably enhanced the OER performance of $Mn_{0.2}RuO_2$ in acidic solutions. Experimental data and DFT simulations inferred that this reaction pathway change was related to the microstructural change from Ru-O-Ru to $Mn^{4-\delta}$-O-$Ru^{4+\delta}$, exhibiting better electron redistribution between the Mn/Ru pair as compared to the Ru/Ru pair in RuO_2. In this case, the direct connection of *O atoms on Mn/Ru atoms was considerably easier than forming *OOH species on one metallic site. Additionally, the electron redistribution in the $Mn^{4-\delta}$-O-$Ru^{4+\delta}$ increased the electrical conductivity of the material, facilitating the adsorption of *OH species and the desorption of the products, which imparted better stability to $Mn^{4-\delta}$-O-$Ru^{4+\delta}$ in acid as compared to that of Ru-O-Ru. Therefore, this study confirmed that the OPM pathway could not be attributed only to the distance between two nearby active host centers. The primary factor for inducing an OPM pathway was the existence of a suitable microstructure where electrons could be delocalized between two active centers. Consequently, OER catalysts could be reasonably predicted and artificially designed with suitable microstructures that preferentially follow the OPM pathway.

Methods

Chemical and materials

Ruthenium chloride anhydrous ($RuCl_3$, AR), Manganese nitrate tetrahydrate ($Mn(NO_3)_2 \cdot 4H_2O$, AR), urea (AR), glucose (AR), commercial RuO_2 (AR), commercial Pt/C (AR), and heavy-oxygen water ($H_2^{18}O$, 97 atom % ^{18}O) were purchased from Aladdin Co., Ltd. Nafion solution (AR) was purchased from Sigma-Aldrich. Sulfuric acid (AR), Hydrogen peroxide 30% aqueous solution (H_2O_2, AR), and ethanol (AR) were purchased from Shanghai Research Institute of Chemical Industry. Nafion 115 membrane (N115, thickness = 127 μm) was purchased from Dupont. Polytetrafluoroethylene (PTFE) membrane (porosity ≥ 50%, pore size ≤ 20 nm, thickness = 40 μm) was provided by Linglu Instruments Shanghai. All chemicals were used without further purification.

Synthesis of catalysts

In a typical procedure, 2 g urea and 10 g glucose were mixed in 10 mL deionized water. The mixture was subjected to ultrasound for 30 minutes until a homogeneous solution was obtained. Subsequently, 20 mg $Mn(NO_3)_2 \cdot 4H_2O$ and 83 mg $RuCl_3$ were added to the solution, and the solution was stirred for 30 minutes to obtain a uniform colloidal suspension. Then, the solution was sealed and heated at 150 °C for 10 hours, forming a porous foam. Finally, the foam was annealed in a muffle furnace at 500 °C for 15 hours to prepare the $Mn_{0.2}RuO_2$ nanorods. The same preparation process was also used to prepare p-RuO_2, $Mn_{0.1}RuO_2$ and $Mn_{0.3}RuO_2$ with different amounts of $Mn(NO_3)_2 \cdot 4H_2O$ added.

Characterization

Both the SEM and TEM results are measured at the Experimental Center of Engineering and Materials Science, University of Science and Technology of China. The SEM images were captured by Gemini SEM 500, while JEM-2100F was used to acquire the TEM, HRTEM, and EDS mapping images. The XRD patterns were obtained using a Philips X'Pert Pro Super diffractometer with Cu Kα radiation (λ = 1.54178 Å) in the 2θ range of 20-80°. The concentration of dissolved metal in the electrolyte of the samples were determined by ICP-MS (Plasma Quad). Electron paramagnetic resonance spectra were generated using the Japan JES-FA 200 (JEOL) spectrometer. Atomic scale HADDF-STEM images, EELS spectra, and atomic scale mapping images were obtained using the Thermo Fisher Scientific Themis Z. The XPS signals of the samples were collected using a Thermo NEXSA G2 spectrometer equipped with an Al-Kα (hυ = 1486.6 eV) X-ray source at Instrument Center for Physical Science, University of Science and Technology of China[51].

Electrochemical measurements

In a typical test, a mixture consisting of 0.75 mL of deionized water, 0.25 mL of ethanol, 0.03 mL of Nafion solution, and 5 mg of sample was sonicated for 1 hour to prepare a well-dispersed catalyst ink. For the preparation of the working electrode, 5 μL of catalyst ink was uniformly deposited onto a freshly polished glassy-carbon electrode (GCE) with a diameter of 0.3 cm, corresponding to a catalyst loading of 0.34 mg cm^{-2}. The target electrolyte solution was prepared by diluting analytical-grade sulfuric acid in a brown volumetric flask, ensuring it was freshly prepared and promptly used. The calibration reference electrode process was as follows: Two Pt wires served as the working and counter electrodes, respectively, with Ag/AgCl being calibrated as the reference electrode, and H_2-saturated 0.5 M H_2SO_4 solution was employed as the electrolyte[52]. The corrected reference electrode potential value was obtained through CV cycles performed near the open circuit voltage. In the standard three-electrode system, the GCE, Pt wire, and Ag/AgCl were utilized as the working, counter, and reference electrodes, respectively. In this work, OER measurements were conducted in an O_2-saturated 0.5 M H_2SO_4 electrolyte (pH = 0) using a CHI 760E electrochemical workstation at room temperature. The measured potentials were recorded versus the reference electrode and converted to reversible hydrogen electrode (RHE) following the relationship: E (V vs. RHE) = E (Ag/AgCl) + 0.059 pH + 0.197 V. OER polarization curves were corrected with *iR*-compensation following the formula: Potential (V vs. RHE) = E (V vs. RHE) − *iR*, where *i* represents current and *R* denotes the uncompensated ohmic resistance of the electrolyte. The *iR*-compensation was executed through on-the-fly correction, an automatic correction mode based on positive feedback, with the compensation level set to 85% unless otherwise specified. The *R* value for commercial RuO_2 within this system was measured to be ~2 ohms (Supplementary Fig. 43). The Nyquist plots for all samples were measured at the same potential value with an amplitude of 5 mV and frequencies ranging from 100 kHz to 0.1 Hz. The ECSA of the catalyst was estimated by determining the double-layer capacitance (C_{dl}) derived from the CV curves within a non-Faradaic potential window at a series of different scan rates of 10, 20, 30, 40, and 50 mV s^{-1}. The ECSA was proportional to the C_{dl}[53]. Stability testing was conducted at a constant current density of 10 and 50 mA cm^{-2} using a CHI 760E electrochemical workstation.

PEMWE measurements

The catalysts-coated membrane (CCM) process was employed to prepare the membrane electrode assembly (MEA) for the PEM electrolyzer. Before the construction of CCM, N115 membrane was treated with H_2O_2, deionized water, and 0.5 M H_2SO_4 at 80 °C for 1 hour, respectively. The treated N115 membrane was stored in deionized water. The anode catalyst ink consisted of synthesized p-RuO_2 and

$Mn_{0.2}RuO_2$, ionomer (D2020), and dispersing solution. In detail, the anode catalyst ($5\ mg\ mL^{-1}$) was added to a mixed solution of water and isopropanol ($V_{water}: V_{isopropanol} = 1:3$) and sonicated for 30 minutes to ensure complete wetting of the catalyst. Subsequently, 10 wt % ionomer was incorporated into the dispersion, followed by another 30 minutes to prepare the anode catalyst ink. The cathode catalyst ink (commercial Pt/C, $5\ mg\ mL^{-1}$) was obtained by the same procedure. Afterwards, the catalysts were uniformly sprayed onto the proton exchange membrane using the ultrasonic spraying method to form the CCM for the PEM electrolyzer. Pt-coated Ti felts were used as the porous transport layer (PTL) for both the cathode and anode in the construction of the CCM electrolyzer. The effective active area of the electrolyzer was $5\ cm^2$ ($2\ cm \times 2.5\ cm$). The PEM electrolyzers were operated at $60\ °C$, with deionized water as the reactant at an inlet flow rate of $10\ mL\ min^{-1}$ (recirculated by a peristaltic pump). Polarization curves were examined over the range of $0–3\ A\ cm^{-2}$, and stability was assessed using the timed current curves at $200\ mA\ cm^{-2}$.

XAFS measurements

Mn K-edge and Ru K-edge XAFS spectra were collected at the 1W1B and BL13SSW beamline stations of the Beijing synchrotron radiation facility (BSRF) and Shanghai synchrotron radiation facility (SSRF), respectively. The positions of the absorption edges were calibrated using Mn foil and Ru foil standard samples. Operando XAFS spectra of $Mn_{0.2}RuO_2$ were collected using a custom-built electrochemical cell. A thin carbon paper loaded with $Mn_{0.2}RuO_2$ catalyst served as the working electrode, while Pt wire and Ag/AgCl were used as the counter and reference electrodes, respectively. To prevent electrolyte leakage and ensure accurate sample detection, Kapton film was applied to the opening window of the electrochemical cell (Supplementary Fig. 44)[54]. During the OER process, potentials ranging from OCP to 1.5 V vs. RHE were applied under constant voltage, and the XAFS spectra were collected using fluorescence mode. The Mn K-edge and Ru K-edge EXAFS spectra were processed using the ATHENA module of the IFEFFIT software package. Additionally, the O K-edge, Ru M-edge, and Mn L-edge XANES spectra were collected at the BL12B beamline station of the National synchrotron radiation laboratory (NSRL), while the Ru L_3-edge XANES spectra were obtained at the BL16U1 beamline station of the SSRF.

SR-FTIR measurements

Operando SR-FTIR experiments were conducted at the BL01B beamline station of NSRL using a custom-built cell (Supplementary Fig. 44)[55,56]. The p-RuO_2 and $Mn_{0.2}RuO_2$ catalysts were loaded onto a GCE embedded in the center of the cell, while Pt wire and Ag/AgCl were served as the counter and reference electrodes, respectively. To prevent electrolyte evaporation from damaging the microscope lens, a BaF_2 window was placed aboved the cell. During the OER process, potentials were applied from OCP to 1.5 V vs. RHE under constant voltage, and the SR-FTIR spectra were recorded by averaging 126 scans at a resolution of $1\ cm^{-1}$.

DEMS with isotope labeling

Operando DEMS with isotope labeling measurements were carried out using the QAS 100 device (Linglu Instruments, Shanghai). The p-RuO_2 and $Mn_{0.2}RuO_2$ catalyst ink ($5\ mg\ mL^{-1}$) were directly deposited onto the Au film sputtered onto a porous PTFE membrane, which served as the working electrode. The hydrophobic PTFE membrane allows gas flow while rejecting liquid (Supplementary Fig. 44). A saturated Ag/AgCl electrode and Pt wire were used as reference electrode and counter electrode, respectively. For the isotope labeling studied, 2 mL $0.5\ M\ H_2SO_4$ solution was prepared using $H_2^{18}O$ (97 atom % ^{18}O) as the solvent. The p-RuO_2 and $Mn_{0.2}RuO_2$ catalysts were subjected to three LSV cycles within the potential range of 1.0–1.6 V vs RHE at a scan rate

of $10\ mV\ s^{-1}$. The mass signals of different molecular weight gas products were recorded in real-time, including $^{32}O_2$ ($^{16}O^{16}O$), $^{34}O_2$ ($^{16}O^{18}O$), and $^{36}O_2$ ($^{18}O^{18}O$). Before the electrochemical measurements, the electrolyte was purged with high-purity Ar gas to remove the dissolved oxygen.

Theoretical calculation details

First-principles calculations were carried out using the Vienna Ab-initio Simulation Package (VASP) code. To enhance calculation efficiency, projector augmented wave (PAW) pseudo-potentials were employed to treat the core electrons, and the Perdew, Burke, and Ernzernhof (PBE) functional was used for exchange-correlation corrections[57–60]. A plane-wave cut-off energy of 450 eV was set to expand the electron wave functions. The convergence criteria for the electronic self-consistent iteration and the maximum force on each atom were set to $10^{-5}\ eV$ and $0.02\ eV\ Å^{-1}$, respectively. During the structural and electronic calculations, K points grids of $3 \times 3 \times 1$ and $5 \times 5 \times 1$ in the Brillouin zone were generated automatically using the Gamma center method. An effective U-J value of 4.00 eV was applied for Mn atom[61,62].

Data availability

The data that support the conclusion of this study are available within the paper and Supplentary Information. Source data are provided with this paper.

References

1. Seh, Z. W. et al. Combining theory and experiment in electrocatalysis: insights into materials design. *Science* **355**, 6321 (2017).
2. Turner, J. A. Sustainable hydrogen production. *Science* **305**, 972–974 (2004).
3. Mallapaty, S. How China could be carbon neutral by mid-century. *Nature* **586**, 482–483 (2020).
4. Shi, Z. et al. Customized reaction route for ruthenium oxide towards stabilized water oxidation in high-performance PEM electrolyzers. *Nat. Commun.* **14**, 843 (2023).
5. Wu, Z. Y. et al. Non-iridium-based electrocatalyst for durable acidic oxygen evolution reaction in proton exchange membrane water electrolysis. *Nat. Mater.* **22**, 100–108 (2023).
6. Chen, Z. et al. Advances in Oxygen evolution electrocatalysts for proton exchange membrane water electrolyzers. *Adv. Energy Mater.* **12**, 2103670 (2022).
7. Rao, R. R. et al. Operando identification of site-dependent water oxidation activity on ruthenium dioxide single-crystal surfaces. *Nat. Catal.* **3**, 516–525 (2020).
8. Cherevko, S. et al. Oxygen and hydrogen evolution reactions on Ru, RuO_2, Ir, and IrO_2 thin film electrodes in acidic and alkaline electrolytes: a comparative study on activity and stability. *Catal. Today* **262**, 170–180 (2016).
9. Qin, Y. et al. RuO_2 electronic structure and lattice strain dual engineering for enhanced acidic oxygen evolution reaction performance. *Nat. Commun.* **13**, 3784 (2022).
10. Sun, S. C. et al. Bifunctional WC-supported RuO_2 nanoparticles for robust water splitting in acidic media. *Angew. Chem. Int. Ed.* **61**, e202202519 (2022).
11. Wohlfahrt Mehrens, M. et al. Oxygen evolution on Ru and RuO_2 electrodes studied using isotope labelling and on-line mass spectrometry. *J. Electroanal. Chem.* **237**, 251–260 (1987).
12. Huang, Z. F. et al. Tuning of lattice oxygen reactivity and scaling relation to construct better oxygen evolution electrocatalyst. *Nat. Commun.* **12**, 3992 (2021).
13. Huang, Z.-F. et al. Strategies to break the scaling relation toward enhanced oxygen electrocatalysis. *Matter* **1**, 1494–1518 (2019).
14. Man, I. C. et al. Universality in oxygen evolution electrocatalysis on oxide surfaces. *ChemCatChem* **3**, 1159–1165 (2011).

15. Yao, Y. et al. Engineering the electronic structure of single atom Ru sites via compressive strain boosts acidic water oxidation electro-catalysis. *Nat. Catal.* **2**, 304–313 (2019).

16. Klyukin, K. et al. Role of dissolution intermediates in promoting oxygen evolution reaction at RuO₂ (110) surface. *J. Phys. Chem. C.* **123**, 22151–22157 (2019).

17. Kötz, R. & Stucki, S. et al. In-situ identification of RuO₄ as the cor-rosion product during oxygen evolution on ruthenium in acid media. *J. Electroanal. Chem.* **172**, 211–219 (1984).

18. Zagalskaya, A. et al. Role of defects in the interplay between adsorbate evolving and lattice oxygen mechanisms of the oxygen evolution reaction in RuO₂ and IrO₂. *ACS Catal.* **10**, 3650–3657 (2020).

19. Wang, K. et al. Highly active ruthenium sites stabilized by mod-ulating electron-feeding for sustainable acidic oxygen-evolution electrocatalysis. *Energy Environ. Sci.* **15**, 2356–2365 (2022).

20. Yao, N. et al. Atomically dispersed Ru oxide catalyst with lattice oxygen participation for efficient acidic water oxidation. *Chem* **9**, 1882–1896 (2023).

21. Lang, C. et al. Observation of a potential-dependent switch of water-oxidation mechanism on Co-oxide-based catalysts. *Chem* **7**, 2101–2117 (2021).

22. Lin, C. et al. In-situ reconstructed Ru atom array on α-MnO₂ with enhanced performance for acidic water oxidation. *Nat. Catal.* **4**, 1012–1023 (2021).

23. Song, F. et al. An unconventional iron nickel catalyst for the oxygen evolution reaction. *ACS Cent. Sci.* **5**, 558–568 (2019).

24. Chen, S. et al. Reconstructed Ir–O–Mo species with strong Brønsted acidity for acidic water oxidation. *Nat. Commun.* **14**, 4127 (2023).

25. Wang, N. et al. Doping shortens the metal/metal distance and promotes OH coverage in non-noble acidic oxygen evolution reaction catalysts. *J. Am. Chem. Soc.* **145**, 7829–7836 (2023).

26. Zhou, C. et al. Superdurable bifunctional oxygen electrocatalyst for high-performance zinc–air batteries. *J. Am. Chem. Soc.* **144**, 2694–2704 (2022).

27. Hao, S. et al. Dopants fixation of Ruthenium for boosting acidic oxygen evolution stability and activity. *Nat. Commun.* **11**, 5368 (2020).

28. Niu, S. et al. Se-doping activates FeOOH for cost-effective and efficient electrochemical water oxidation. *J. Am. Chem. Soc.* **141**, 7005–7013 (2019).

29. Dang, Q. et al. Iridium metallene oxide for acidic oxygen evolution catalysis. *Nat. Commun.* **12**, 6007 (2021).

30. Zhao, Z. L. et al. Boosting the oxygen evolution reaction using defect-rich ultra-thin ruthenium oxide nanosheets in acidic media. *Energy Environ. Sci.* **13**, 5143–5151 (2020).

31. Geiger, S. et al. The stability number as a metric for electrocatalyst stability benchmarking. *Nat. Catal.* **1**, 508–515 (2018).

32. He, J. et al. Regulating electron redistribution of intermetallic iri-dium oxide by incorporating Ru for efficient acidic water oxidation. *Adv. Energy Mater.* **11**, 2102883 (2021).

33. Wang, J. et al. Exceptionally active and stable RuO₂ with interstitial carbon for water oxidation in acid. *Chem* **8**, 1673–1687 (2022).

34. Chen, D. et al. Ionothermal route to phase-pure RuB₂ catalysts for efficient oxygen evolution and water splitting in acidic media. *ACS Energy Lett.* **5**, 2909–2915 (2020).

35. Cui, X. et al. Robust interface Ru centers for high-performance acidic oxygen evolution. *Adv. Mater.* **32**, e1908126 (2020).

36. Rong, C. et al. Electronic structure engineering of single-atom Ru sites via Co-N4 sites for bifunctional pH-universal water splitting. *Adv. Mater.* **34**, e2110103 (2022).

37. Yao, Q. et al. Channel-rich RuCu nanosheets for pH-universal overall water splitting electrocatalysis. *Angew. Chem. Int. Ed.* **58**, 13983–13988 (2019).

38. Yin, J. et al. Iridium single atoms coupling with oxygen vacancies boosts oxygen evolution reaction in acid media. *J. Am. Chem. Soc.* **142**, 18378–18386 (2020).

39. Yeo, K.-R. et al. A highly active and stable 3D dandelion spore-structured self-supporting Ir-based electrocatalyst for proton exchange membrane water electrolysis fabricated using structural reconstruction. *Energy Environ. Sci.* **15**, 3449–3461 (2022).

40. Wang, H. et al. Significantly enhanced overall water splitting performance by partial oxidation of ir through au modification in core–shell alloy structure. *J. Am. Chem. Soc.* **143**, 4639–4645 (2021).

41. Zhang, N. et al. Metal substitution steering electron correlations in pyrochlore ruthenates for efficient acidic water oxidation. *ACS Nano* **15**, 8537–8548 (2021).

42. Yang, J. et al. A universal strategy to metal wavy nanowires for efficient electrochemical water splitting at pH-universal conditions. *Adv. Funct. Mater.* **28**, 1803722 (2018).

43. Chang, J. et al. Oxygen radical coupling on short-range ordered Ru atom arrays enables exceptional activity and stability for acidic water oxidation. *J. Am. Chem. Soc.* **146**, 12958–12968 (2024).

44. Yu, H. et al. Strain-triggered distinct oxygen evolution reaction pathway in two-dimensional metastable phase IrO₂ via CeO₂ load-ing. *J. Am. Chem. Soc.* **146**, 20251–20262 (2024).

45. Wang, B. et al. In situ structural evolution of the multi-site alloy electrocatalyst to manipulate the intermediate for enhanced water oxidation reaction. *Energy Environ. Sci.* **13**, 2200–2208 (2020).

46. Zhou, W. et al. Regulating the scaling relationship for high catalytic kinetics and selectivity of the oxygen reduction reaction. *Nat. Commun.* **13**, 6414 (2022).

47. Hu, C. et al. Inhibiting demetalation of Fe—N—C via Mn sites for efficient oxygen reduction reaction in zinc-air batteries. *Adv. Mater.* **36**, 2405763 (2024).

48. Shi, Z. et al. Confined Ir single sites with triggered lattice oxygen redox: toward boosted and sustained water oxidation catalysis. *Joule* **5**, 2164–2176 (2021).

49. Xue, Y. et al. Stabilizing ruthenium dioxide with cation-anchored sulfate for durable oxygen evolution in proton-exchange mem-brane water electrolyzers. *Nat. Commun.* **14**, 8093 (2023).

50. Bordiga, S. et al. Reactivity of surface species in heterogeneous catalysts probed by In Situ x-ray absorption techniques. *Chem. Rev.* **113**, 1736–1850 (2013).

51. Gu, C. et al. Tuning electronic structure of metal-free dual-site catalyst enables exclusive singlet oxygen production and in-situ utilization. *Nat. Commun.* **15**, 5771 (2024).

52. Li, L. et al. Lanthanide-regulating Ru-O covalency optimizes acidic oxygen evolution electrocatalysis. *Nat. Commun.* **15**, 4974 (2024).

53. Zhu, J. et al. Activating inert sites in cobalt silicate hydroxides for oxygen evolution through atomically doping. *Energy Environ. Mater.* **5**, 655–661 (2022).

54. Kang, J. et al. Valence oscillation and dynamic active sites in monolayer NiCo hydroxides for water oxidation. *Nat. Catal.* **4**, 1050–1058 (2021).

55. Tang, B. et al. A Janus dual-atom catalyst for electrocatalytic oxygen reduction and evolution. *Nat. Synth.* **3**, 878–890 (2024).

56. Zhou, W. et al. Self-synergistic cobalt catalysts with symbiotic metal single-atoms and nanoparticles for efficient oxygen reduction. *J. Mater. Chem. A* **9**, 1127–1133 (2021).

57. Perdew, J. et al. Generalized gradient approximation made simple. *Phys. Rev. Lett.* **77**, 3865–3868 (1996).

58. Kresse, J. et al. Efficiency of ab-initio total energy calculations for metals and semiconductors using a plane-wave basis set. *Comput. Mater. Sci.* **6**, 15–50 (1996).

59. Hafner, J. Ab-initio simulations of materials using VASP: density-functional theory and beyond. *J. Comput. Chem.* **29**, 2044–2078 (2008).

60. Cao, F. Interfacial engineering of $CuWO_4$/WO_3 thin films precisely fabricated by ultrasonic spray pyrolysis for improved solar water splitting. *Catal. Sci. Technol.* **13**, 4550–4557 (2023).

61. Zhao, C. et al. Cooperative catalysis toward oxygen reduction reaction under dual coordination environments on intrinsic $AMnO_3$-type perovskites via regulating stacking configurations of coordination units. *Adv. Mater.* **32**, 2006145 (2020).

62. Deng, L. et al. ZnO/ZnS heterostructure with enhanced interfacial lithium absorption for robust and large-capacity energy storage. *Energy Environ. Sci.* **15**, 4738–4747 (2022).

Acknowledgements

Author contributions

X.C. and W.Y. conceived the project. Q.J. conducted the experiments. X.Z. and C.W. performed the theoretical modeling. B.T. and J.Z. helped with the synchrotron experiments. Q.J. and B.T. synthesized and characterized the samples. Q.J. and B.T. analyzed the data. Q.J., X.C., and W.Y. wrote the manuscript. H.T. and C.W. gave input during the writing process. R.L., M.S., H.L., and C.J. together performed the electron microscopy imaging, SR-FTIR, and Faradic efficiency characterizations.

Competing interests

All authors declared no conflict of interest.

Additional information